Backbone Dynamics of *Escherichia coli* Adenylate Kinase at the Extreme Stages of the Catalytic Cycle Studied by ^{15}N NMR Relaxation†

Yury E. Shapiro,‡ Michael A. Sinev,‡ Elena V. Sineva,‡ Vitali Tugarinov,§ and Eva Meirovitch*,‡

Faculty of Life Sciences, Bar-Ilan University, Ramat-Gan 52900, Israel, Department of Structural Biology, The Weizmann Institute of Science, Rehovot 76100, Israel

Received September 3, 1999; Revised Manuscript Received March 16, 2000

ABSTRACT: Adenylate kinase from *Escherichia coli* (AKeco), consisting of a single 23.6 kDa polypeptide chain folded into domains CORE, AMPbd, and LID, catalyzes the reaction AMP + ATP → 2ADP. Domains LID and AMPbd execute large-scale movements during catalysis. Backbone dynamics of ligand-free and AP_5A-inhibitor-bound AKeco were studied comparatively with ^{15}N NMR relaxation methods. Overall diffusion with correlation times of 15.05 (11.42) ns and anisotropy $D_{parallel}/D_{perp} = 1.25$ (1.10), and fast internal motions with correlation times up to 100 ps (50 ps), were determined for AKeco (AKeco*AP_5A). Fast internal motions affect 93% of the AKeco sites, with pronounced preference for domains AMPbd and LID, and 47% of the AKeco*AP_5A sites, with limited variability along the chain. The mean squared generalized order parameters, $\langle S^2 \rangle$, of secondary structure elements and loops are affected by ligand binding differentially and in a domain-specific manner. Nanosecond motions predominate within AMPbd. Prominent exchange contributions, associated in particular with residue G10 of the nucleotide-binding P-loop motif, are interpreted to reflect hydrogen-bond dynamics at the inhibitor-binding site. The hypothesis of energetic counter balancing of substrate binding based on crystallographic data is strongly supported by the solution NMR results. Correlations between backbone dynamics and domain displacement are established.

The existence of a close relationship between protein function and dynamic structure is nowadays widely acknowledged (*1*). Allosteric effects associated with multiple-domain proteins are good examples of this correlation. Understanding the role of domains in molecular recognition is of great interest (*2*, *3*), and the issue of domain flexibility in solution is a general one for large multiple-domain proteins (*4*). The structural, dynamic, and binding properties of the individual domains are often fairly well understood. On the other hand, the structural organization, interdomain interactions, and domain mobility associated with the integrated system are complex and difficult to elucidate. However, these aspects are likely to be significant, particularly when ligand binding involves large domain displacements. The study of natural molecular assemblies in solution is often hindered by their prohibitive size, and only smaller mimics are amenable to investigation (*5*).

Adenylate kinase from *Escherichia coli* (AKeco)[1] incorporates *naturally* the features of an archetypal multiple-domain system. The structural flexibility of AKeco facilitates the assembly of an enzymatic reaction center by large-scale motions of entire domains (*1*, *6*). AK is a ubiquitous multiple-domain enzyme that controls the cellular energy balance by catalyzing the transfer of a phosphoryl group from ATP to AMP (*7*). Close to 20 crystal structures of various adenylate (and other nucleoside monophosphate) kinases have been solved thus far (*8*). AKeco is made of a single polypeptide chain folded into domains CORE, AMPbd, and LID (*9*, *10*). A ribbon diagram of the crystal structure of the so-called "open" ligand-free form (*10*) is shown in Figure 1a. CORE is the largest domain. It includes residues M1-I29, T60-V121, and Q160-G214 that form a five-stranded parallel β-sheet comprising strands $\beta_1-\beta_4$ and β_9 surrounded by helices α_1 and $\alpha_4-\alpha_9$. Domain AMPbd includes helices α_2 and α_3 formed by residues S30−V59. The LID domain includes residues G122−D159, which form a four-stranded antiparallel β-sheet (strands $\beta_5-\beta_8$). Domains AMPbd and LID are displaced significantly upon substrate binding (*8*, *11*). The active site is configured thereby, and a "closed" structure is obtained (Figure 1b). It is assumed that following the reaction the structure "opens up" again through reverse movements of AMPbd and LID, to recover the original ligand-free enzyme (*10*). This mechanism has been inferred based on the crystal structures of ligand-free AK enzymes and various molecular complexes with nucleoside monophosphates, nucleoside triphosphates, and inhibitors (*8*).

† This work was supported by a grant from the Israel Science Foundation to E.M. It was also supported in part by Grant RO1GM39372 from the National Institutes of General Medical Sciences and a grant from the Israel Science Foundation to Prof. Elisha Haas from the Faculty of Life Sciences, Bar-Ilan University, Israel, and by the Gruss Foundation.

* To whom correspondence should be addressed. E-mail: eva@nmrsgi1.ls.biu.ac.il. Phone: 972-3-5318049. Fax: 972-3-5351824.

‡ Bar-Ilan University.

§ The Weizmann Institute of Science.

[1] Abbreviations: AK, adenylate kinase; AKeco, adenylate kinase from *Escherichia coli*; ATP, adenosine triphosphate; ADP, adenosine diphosphate; AMP, adenosine monophosphate; AMPbd, AMP-binding domain; AP_5A, P^1,P^5-di(adenosine-5′)pentaphosphate; CSA, chemical shift anisotropy; HSQC, heteronuclear single-quantum coherence; NMR, nuclear magnetic resonance; NOE, nuclear Overhauser enhancement; PDB, protein data bank.

10.1021/bi992076h CCC: $19.00
Published on Web 05/09/2000

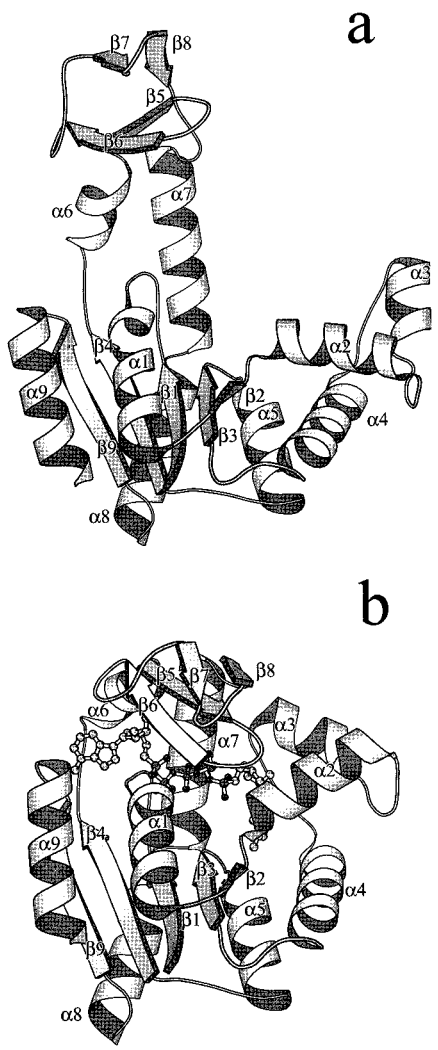

FIGURE 1: Ribbon diagrams of the crystal structure of adenylate kinase from *E. coli* in the ligand-free form (a) and in complex with the two-substrate-mimicking inhibitor AP_5A (b). The figures were drawn with the program Molscript (*71*), using the PDB coordinate files 4ake (molecule II) for AKeco, and 1ake (complex II) for AKeco*AP_5A.

AKeco is the only adenylate kinase for which crystal structures corresponding to the extreme stages of the catalytic cycle are available (*9*, *10*, *12*), with the closed form of AKeco represented by its complex with the two-substrate-mimicking inhibitor AP_5A (*9*, *12*−*14*). The ATP phosphates are bound to the enzyme partly through the so-called P-loop GXXGXGK (AKeco residues 7−13). This binding motif between proteins and nucleotides occurs in many proteins that bind nucleoside triphosphate, in all the nucleoside monophosphate kinases, and in the weakly homologous G-proteins (*9*). When bound to AKeco, the two-substrate mimicking inhibitor AP_5A adopts a conformation close to the suggested transition state (*15*). Thus, we have at hand a prototype for a multiple-domain biological machine, where mobility and function must necessarily be interrelated.

The crystallographic studies provided a clear picture of domain reorganization. Domain CORE appears to form the stable frame of the protein, relative to which the smaller domains are displaced during catalysis (*10*). This model is, however, based on static structures, disregarding altogether dynamic aspects. Domain closure in solution was confirmed recently by time-resolved energy transfer studies of AKeco derivatives labeled with fluorescent probes in both the ligand-free and AP_5A-bound forms (*16*, *17*). These studies suggested significant reduction in enzyme flexibility upon inhibitor binding (*16*). Traditional homonuclear (*18*) and heteronuclear (*19*−*23*) solution NMR methods were used in the past to study AK from *E. coli* and other sources. These studies provided only limited structural and dynamic information.

NMR relaxation methods can generate information on molecular motions *in solution* in a comprehensive way, on a variety of time scales, and at the atomic level (*24*). To correlate the dynamic properties of AKeco with ligand binding and domain displacement it is necessary to apply these methods to both the ligand-free and ligand-bound forms and conduct a thorough comparative investigation. Here, we report on backbone dynamics of AKeco studied with ^{15}N relaxation, and present a comparison between the ensuing dynamic states of the ligand-free and AP_5A-bound enzyme forms. Differences in the respective hydrodynamic and microdynamic properties are pinpointed. Binding-induced changes in ^{15}N relaxation parameters are elucidated at the level of individual domains, as well as secondary structure elements within each domain. Correlations between backbone dynamics and catalysis-related domain displacement are established.

THEORETICAL BACKGROUND

Relaxation of an amide ^{15}N nucleus spin at high field is dominated by the dipolar interaction with the directly attached proton spin and by the ^{15}N chemical shift anisotropy (CSA), $\Delta\sigma$. Spin−lattice (R_1) and spin−spin (R_2) relaxation rates, and ^{15}N-{^1H} steady-state NOE are given by (*25*)

$$R_1 = (d^2/4)[J(\omega_H - \omega_N) + 3J(\omega_N) + 6J(\omega_H + \omega_N)] + c^2J(\omega_N) \quad (1)$$

$$R_2 = (d^2/8)[4J(0) + J(\omega_H - \omega_N) + 3J(\omega_N) + 6J(\omega_H) + 6J(\omega_H + \omega_N)] + (c^2/6)[4J(0) + 3J(\omega_N)] + R_{ex} \quad (2)$$

$$\mathrm{NOE} = 1 + (d^2/4R_1)(\gamma_H/\gamma_N)[6J(\omega_H + \omega_N) - J(\omega_H - \omega_N)] \quad (3)$$

where $d = (\mu_0 h\gamma_N\gamma_H/8\pi^2)\langle r_{NH}^{-3}\rangle$, $c = \omega_N\Delta\sigma/\sqrt{3}$, μ_0 is the permeability of free space; h is Planck's constant; γ_H and γ_N are the magnetogyric ratios of ^1H and ^{15}N, respectively; $r_{NH} = 1.02$ Å is the mean nitrogen−hydrogen bond length; $J(\omega)$ denotes the spectral density function; ω_H and ω_N are the Larmor frequencies of ^1H and ^{15}N, respectively. The phenomenological R_{ex} term in eq 2 represents conformational exchange and pseudo-first-order processes occurring on the microsecond to millisecond time scale (*26*).

The amplitudes and time scales of the intramolecular motions experienced by the protein backbone are commonly determined from the relaxation data by using the model-free approach suggested by Lipari and Szabo (*27*, *28*) and extended by Clore et al. (*29*, *30*). In this analysis, the spectral density function, $J(\omega)$, is modeled as

$$J(\omega) = \frac{2}{5}\{[S^2\tau_m/(1 + (\omega\tau_m)^2)] + [(1 - S_f^2)\tau_f'/(1 + (\omega\tau_f')^2)] + [(S_f^2 - S^2)\tau_s'/(1 + (\omega\tau_s')^2)]\} \quad (4)$$

where $\tau_f' = \tau_f\tau_m/(\tau_f + \tau_m)$; $\tau_f' = \tau_s\tau_m/(\tau_s + \tau_m)$, τ_m is the correlation time for overall isotropic rotational reorientation, τ_f is the effective correlation time for internal motions on a fast time scale (typically $\tau_f < 100$ ps), τ_s is the effective correlation time for internal motions on a slow time scale ($\tau_f < \tau_s < \tau_m$), $S^2 = S_f^2S_s^2$ is the square of the generalized order parameter characterizing the amplitude of the internal motions ($0 \leq S^2 \leq 1$), and S_f^2 and S_s^2 are the squares of the order parameters for the internal motions on the fast and slow time scales, respectively. Motions characterized by the generalized order parameter S^2 will be referred to as dynamics on the picosecond to nanosecond time scale. Motions associated with S_f^2 will be referred to as subnanosecond motions and those associated with S_s^2 as nanosecond motions.

Recently, it was shown that ^{15}N NMR relaxation data can be used to determine diffusion tensors of symmetry lower than spherical, e.g., by direct fitting of R_2/R_1 ratios of rigid spins (*31*, *32*). An alternative method, applicable to proteins with relatively small diffusion anisotropy, is the local diffusion constant approach of Brüschweiler et al. (*33*). Using eqs 1, 2, and 4 under the conditions $S_s^2 = 1$ and $\tau_f \rightarrow 0$, and $(R_2/R_1)_i$ ratios of rigid spins, the diffusion tensor can be determined by solving the equation (*34*):

$$D_i = e_i^T\mathbf{A}\mathbf{D}\mathbf{A}^{-1}e_i \quad (5)$$

where e_i is the unit vector defining the orientation of the ith N−H bond vector in a fixed molecular (i.e., inertia) reference frame of a known structure, and **A** is the transformation matrix relating the inertia and diffusion frames. **D** is a diagonal matrix with principal values $(Dyy + Dzz)/2$, $(Dxx + Dzz)/2$, and $(Dxx + Dyy)/2$. For axial symmetry, found to be applicable in this study, $Dxx = Dyy = D_{perp}$, $Dzz = D_{parallel}$, and **A** is given by two Euler angles, θ and ϕ. An apparent correlation time for overall rotational reorientation, $\tau_m(app) = 1/(6 \times D_{iso})$, can be defined, with $D_{iso} = (1/3) \times (Dxx + Dyy + Dzz)$. The parameters D_{iso}, $D_{parallel}/D_{perp}$, θ and ϕ are subsequently incorporated into the calculation of the microdynamic parameters by replacing the first term in eq 4 with expressions appropriate for axial diffusion. For $\omega\tau \gg 1$, $\mathbf{D}_i$ is linear in $Y_{20}(\theta_i)$, where Y_{20} is the reduced second rank spherical harmonic function. This relationship can be used to estimate the distribution of the N−H bond vectors (*34*).

EXPERIMENTAL PROCEDURES

Sample Preparation. For preparation of uniformly ^{15}N-labeled AKeco, *E. coli* HB101 cells, transformed with pEAK91 plasmid, were grown at 37 °C in Celtone-N medium (Martek Biosciences Corp.) containing >98% ^{15}N. The recombinant plasmid pEAK91 contained the intact gene coding for *E. coli* adenylate kinase (*35*). The previously described procedure for purification of AKeco (*17*) was improved by application of Blue-Sepharose affinity chromatography (*35*), followed by size-exclusion chromatography on a Sephacryl S-100 column (Pharmacia). The use of the additional chromatographic step enhanced the yield of the purified enzyme up to 110 mg/L of cell culture.

NMR samples of AKeco in the ligand-free form and in complex with the inhibitor AP_5A were prepared. A stock solution of AKeco was prepared by thorough dialysis of the protein solution against 40 mM sodium-phosphate buffer (pH 6.8) containing 10 μM sodium azide, followed by concentration on a Centricon-10 concentrator (Amicon). Concentration of the AKeco solution was determined by using the absorption coefficient $A_{277nm} = 0.5$ $(mg/mL)^{-1}$ cm^{-1} (*36*). An appropriate amount of the AP_5A (Boehringer, Germany) inhibitor stock solution (pH 6.8) and 50% D_2O, prepared in the same buffer, were added to the concentrated AKeco solution to obtain fully saturated enzyme. The ligand-free sample contained 1.75 mM ^{15}N-labeled enzyme and 40 mM sodium phosphate buffer in 95% H_2O/5% D_2O. The ligand-bound sample contained 2 mM ^{15}N-labeled enzyme, 2.5 mM AP_5A, and 40 mM sodium phosphate buffer in 95% H_2O/5% D_2O. The protein samples were degassed and transferred to 5 mm NMR Shigemi cells.

Size-exclusion chromatography experiments were carried out on the ligand-free enzyme in the context of investigating possible molecular association. Chromatographic runs on a preparative Sephacryl S-100 HR column in 40 mM sodium phosphate buffer (pH 6.8) at 25 °C revealed a single elution peak appearing at the expected monomer position. The position of this peak was found to be independent of the loaded protein concentration in the 0.2−3.4 mM range. On the basis of deliberate dimer generation using the single-cysteine mutant C203-AKeco, the threshold for dimer detection was set at approximately 2%.

NMR Spectroscopy. NMR experiments were carried out at 303 K on a Bruker DMX-600 Avance spectrometer operating at 600.13 MHz ^{1}H frequency and at 60.811 MHz ^{15}N frequency, using a 5 mm ^{1}H-^{13}C-^{15}N triple resonance inverse detection probe. NMR data were analyzed using the software packages nmrPipe and modelXY (*37*) on Silicon Graphics workstations.

Relaxation rates R_1 and R_2, and ^{15}N-{^{1}H} NOEs were measured using established inversion recovery (*38*), spin−echo (*39*), and ^{15}N-{^{1}H} steady-state NOE (*40*) pulse sequences (*41*−*43*). For NOE experiments, we used the sequence shown in Figure 1B of Grzesiek and Bax (*43*), which features H_2O flip-back pulses to minimize saturation of water. The ^{15}N CSA−^{15}N-^{1}H dipolar cross-correlation term, η_{xy}, was measured using the sequence of Tjandra et al. (*44*), with a dephasing period $2\Delta = 14$ ms (16 ms) for AKeco (AKeco*AP_5A). Spectral widths were 1824.5 Hz in the F_1 dimension and 9615.4 Hz in the F_2 dimension. The ^{15}N carrier was set at 118.5 ppm and was referenced indirectly to liquid NH_3 (*45*). 360 × 1024 complex points were acquired in the $t_1 \times t_2$ dimensions for each time point.

The R_1 and R_2 measurements were performed using a total of 40 and 48 transients per t_1 experiment, respectively. For the R_1 measurements of AKeco, nine time points were collected, using parametric delays of 15, 127, 247, 367, 487, 647, 807, 1031, and 1287 ms. The experiment was repeated twice for time points 15, 487, and 1287 ms. For the R_1 measurements of AKeco*AP_5A, eight time points were collected, using parametric delays of 133.5, 245.5, 357.5, 485.5, 645.5, 805.5, 997.5, and 1285.5 ms. The experiment was repeated twice for each time point. The delay between scans was set to 1.5 s in all the R_1 measurements. For the R_2 measurements of both ligand-free and AP_5A-bound AKeco, nine time points were collected using parametric delays of 8, 16, 24, 32, 48, 64, 80, 96, and 128 ms. The experiments for time points 8, 24, 64, and 128 ms were repeated twice. The delay between scans was 1.6 s. The data were apodized

with a cosine (cosine-bell) window function in t_1 (t_2). Duplicates were used to calculate average values of, and uncertainties in, the measured peak heights. Phenomenological R_1 and R_2 values and uncertainties were determined by nonlinear least-squares fitting of the experimental data to monoexponential equations, as described in ref *46*.

The NOE values were determined using pairs of spectra recorded in interleaved mode with and without proton presaturation during the recycle delay. A total of 96 transients per t_1 experiment were recorded. The delays between scans were 3.8 and 6.6 s for AKeco and 3.8, 6.6, and 12.1 s for AKeco*AP_5A. Data were processed as described above. The NOE values were recorded in duplicate, and the replicates were used to determine uncertainties and mean values.

Data Analysis. The diffusion tensor for overall rotational reorientation was determined using the local diffusion approach (*33*, *34*), implemented in the Diffusion package developed by Palmer and co-workers (*34*). Properly reduced R_2/R_1 data sets were used as input to these calculations. Orientations of the unit vectors e_i were calculated for AKeco using the atomic coordinates of complex II given in the PDB entry 4ake (*10*) and for AKeco*AP_5A using the atomic coordinates of complex II given in the PDB entry 1ake (*9*). Hydrogen atoms were added using the program X-PLOR 3.1 (*47*). Equation 5 was solved by least squares optimization for anisotropic, axially symmetric, and isotropic diffusion models. Model selection was based on F-statistic testing.

The experimental ^{15}N R_1 and R_2 rate constants and steady-state ^{15}N-{^1H} NOEs were fitted to eqs 1−4. $\Delta\sigma = -160$ ppm (*48*) was used throughout these calculations assuming that site-specific variability of CSA (*49*) and noncollinearity of the principal axes of the CSA and ^1H-^{15}N dipolar tensors (*50*) can be disregarded. The latter assumption is justified by the relatively small anisotropy $D_{parallel}/D_{perp}$ obtained for both AKeco forms. As indicated by a recent study of Kroenke at al. (*51*), large CSA variations along the protein backbone are likely to be negligible at 14.1 T. Since the present analysis is both qualitative and comparative in nature, the absolute value of $\Delta\sigma$ should not affect our major conclusions.

Five simplified dynamic models were derived from eq 4 extended to axial overall diffusion and used to fit the experimental data as described by Mandel et al. (*52*). Each model contained the overall diffusion tensor and three parameters describing internal motions, one of which was a correlation time—either τ_f or τ_s. For convenience, the effective correlation time for internal motions is referred to as τ_e. The dynamic models featured the following subsets of the extended model free parameters: (1) S^2; (2) S^2 and $\tau_e = \tau_f$, (3) S^2 and R_{ex}, (4) S^2, $\tau_e = \tau_f$ and R_{ex}, and (5) S_f^2, S^2, and $\tau_e = \tau_s$. Model 1 is obtained by assuming that $S_s^2 = 1$ and $\tau_f \rightarrow 0$ and is applicable if motions on the slow time scale are negligible, and motions on the fast time scale are very fast (<20 ps). Model 2 is obtained by assuming that $S_s^2 = 1$ and is applicable if motions on the slow internal time scale are negligible. Models 3 and 4 are derived from models 1 and 2, respectively, by inclusion of nonzero R_{ex} in the relaxation model. For models 1−4, $S^2 = S_f^2$. Model 5 is obtained by assuming that $\tau_f \rightarrow 0$. Version 4.0 of the program Modelfree (*46*, *52*) was used to determine the model-free parameters, based on the three experimentally measured quantities R_1, R_2, and NOE. Model selection was based on simulations of χ^2 distributions and *F*-statistic testing. Statistical properties of the model-free parameters were evaluated from Monte Carlo simulations using 500 randomly distributed synthetic data sets.

RESULTS

Superimposed ^1H-^{15}N-HSQC spectra (*53*) of ^{15}N-AKeco and ^{15}N-AKeco*AP_5A, obtained as the first time points of R_2 experiments, are shown in Figure 2. For 24 kDa protein systems, these are well-resolved spectra. HN and ^{15}N assignments for AKeco at 308 K were reported by Burlacu-Miron et al. (*22*). We performed temperature-related adjustments in these assignments by carrying out the experiments described in references (*54*−*57*). HN and ^{15}N assignments for AKeco*AP_5A were determined previously in our laboratory (*58*). The HN-^{15}N correlation maps of AKeco and AKeco*AP_5A shown in Figure 2 differ considerably. Thus, only about 10% of the peaks preserve their position within one line width in each dimension, pointing out significant changes in local structure induced by ligand binding. A total of 203 HN-^{15}N backbone correlations was expected. For the ligand-free form, 16 residues (A11, K13, G14, I21, M53, D76, R131, F137, N138, K145, R157, R167, Y171, M174, A188, and K211) generated peaks that overlapped with other correlations or could not be detected. Complete data sets of R_1, R_2, and ^{15}N-{^1H} NOE could not be obtained for T31, V169, I179, and K184. The following seven peaks were present as overlapped pairs in the NMR spectrum: A8 and H126, E161 and Y133, Y181 and N102, V142 and H172, A37 and I20, D94 and A203, and E210 and Q173. For the AP_5A-bound form of AKeco, the weak peaks of residues G14, I20, K47, and K157 could not be quantified. Complete data sets of R_1, R_2 and ^{15}N-{^1H} NOE could not be obtained for G32, D84, I120, and D159. The following peaks were present as overlapped pairs in the NMR spectrum: Y133 and V196, A37 and E187, Q28 and I101, M34 and S183, T15 and V169, E62 and V125, A38 and K192, E44 and E75, V39 and A49, and V132 and E170. Overlapped peaks were not considered in the overall diffusion calculations but included in the Modelfree calculations with the provision that the respective microdynamic parameters should be interpreted qualitatively. In summary, 169 AKeco data points were available for diffusion tensor calculations, and 187 for Modelfree calculations. The corresponding figures for AKeco*AP_5A were 175 and 199, respectively.

Experimental ^{15}N R_1, R_2, and ^{15}N-{^1H} NOE data are shown as a function of residue number in Figures 3, panels a−c, for AKeco and AKeco*AP_5A. These profiles reflect considerable differences in the dynamic properties of the ligand-free and AP_5A-bound enzyme forms. The 10% trimmed mean values of R_1, R_2, and NOE are 0.86 ± 0.02 s^{-1}, 19.61 ± 0.46 s^{-1}, and 0.73 ± 0.02 for AKeco and 1.12 ± 0.02 s^{-1}, 15.43 ± 0.26 s^{-1}, and 0.80 ± 0.02 for AKeco*AP_5A. Figure 3d features R_2/R_1 ratios with 10% trimmed mean values of 22.6 ± 0.84 for AKeco and 13.82 ± 0.37 for AKeco*AP_5A. In the presence of relatively uniform R_1 profiles (Figure 3a), ^{15}N-{^1H} NOE data reflect primarily high-frequency local motions. As shown in Figure 3c, for AKeco these motions are significantly more effective within AMPbd and LID as compared to CORE, and become quite uniform throughout the protein backbone upon inhibitor binding. Although the NOE data of AKeco*AP_5A are generally high [similar to those measured for oxidized

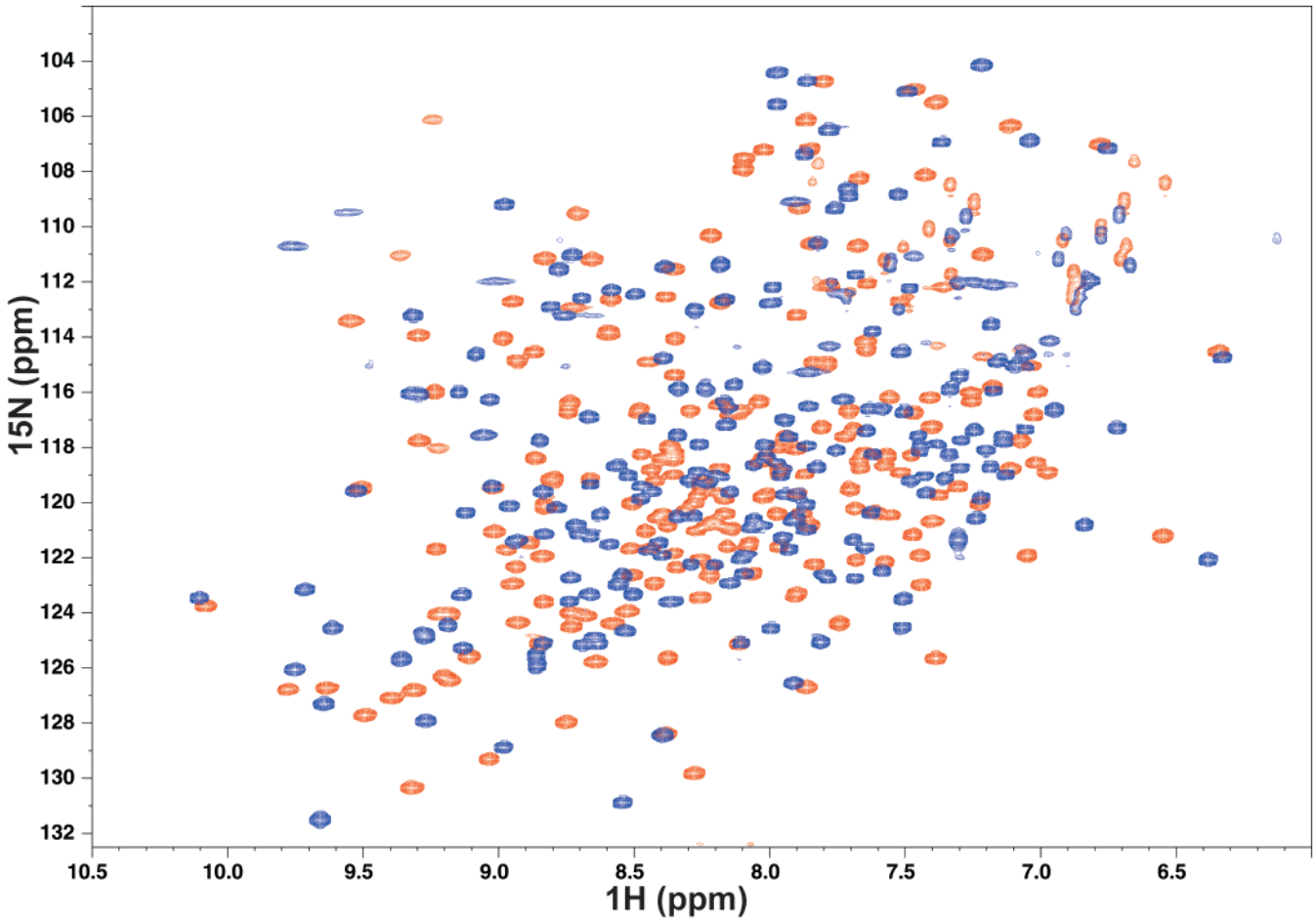

FIGURE 2: Superimposed 600 MHz ^{1}H-^{15}N HSQC spectra of ^{15}N-AKeco (red) and ^{15}N-AKeco*MgAP$_5$A (blue) corresponding to the first (8 ms) points of the R_2 measurements.

flavodoxin by Zhang et al. (*59*)], less than 2% of the NOEs exceeds the rigid-sphere limit at 14.1 T (*60*), if the experimental uncertainty is taken into consideration. The R_2/R_1 profile and, to some extent, the R_2 and ^{15}N-{^{1}H} NOE profiles exhibit an oscillatory pattern scanning extreme values at chain segment Q160−G214.

Overall Diffusion. A diffusion tensor estimate (*34*) was obtained for AKeco*AP$_5$A with an R_2/R_1 input data set including 162 spins, generated with the filtering strategy of Tjandra et al. (*31*). The optimal NOE-filtering threshold, below which spins were omitted from the calculation of the diffusion tensor estimate, while the remaining N−H bond vectors were still distributed in space largely uniformly, was found to be 0.7. The final diffusion tensor, obtained with the Modelfree calculation using this estimate as an initial guess, was given by $D_{iso} = (1.46 \pm 0.01) \times 10^7$ s^{-1}, $D_{parallel}/D_{perp} = 1.10 \pm 0.02$, $\theta = (-0.6 \pm 3.8)°$, and $\phi = (-40.8 \pm 44.4)°$. The values θ and ϕ indicate that the principal axes frames of the diffusion and inertia tensors practically coincide.

Analogous calculations were carried out for the ligand-free enzyme. The optimum R_2/R_1 data set used for diffusion tensor estimation contained 109 spins and was obtained by excluding spins with NOE values below 0.65. The final diffusion tensor was given by $D_{iso} = (1.11 \pm 0.01) \times 10^7$ s^{-1} and $D_{parallel}/D_{perp} = 1.25 \pm 0.02$. The orientation of the principal axes frame of the AKeco diffusion tensor could not be determined with reasonable accuracy and was evaluated as follows. Given that θ and ϕ are nearly zero for AKeco*AP$_5$A, the extreme R_2/R_1 values at chain segment Q160-G214 can be associated with extreme orientations of N−H bond vectors in the AKeco*AP$_5$A crystal structure. As shown in Figure 1b helices α_7 and α_9, and the associated N−H bond vectors, are approximately parallel to the main molecular symmetry axis, whereas helix α_8, the connecting loops, and strand β_9 provide ample opportunities for perpendicular orientations. Figure 1a indicates that these secondary structure elements have similar orientations relative to the main molecular symmetry axis of the AKeco-crystal structure. Therefore, the fact that the oscillatory pattern at chain segment Q160−G214 is also featured by the R_2/R_1 profile of AKeco (Figure 3d) suggests that the orientations of the diffusion and inertia frames are also similar for the ligand-free enzyme. Larger diffusion anisotropy of AKeco as compared to AKeco*AP$_5$A is consistent with larger oscillation amplitude observed with the former at chain segment Q160−G214.

AKeco*AP$_5$A was found to reorient in solution with an apparent correlation time τ_m(app) = 11.42 ns. A Brownian rotational correlation time of 10.11 ns was calculated for a 24 kDa spherical particle surrounded by a single layer of water (*61*). $D_{parallel}/D_{perp} = 1.15$ estimated based on the inertia tensor (*62*) of the crystal structure (a calculation relying intrinsically on the Debye model for rotational reorientation) was found to be similar to $D_{parallel}/D_{perp} = 1.10$ obtained with NMR. The ligand free enzyme was found to reorient in

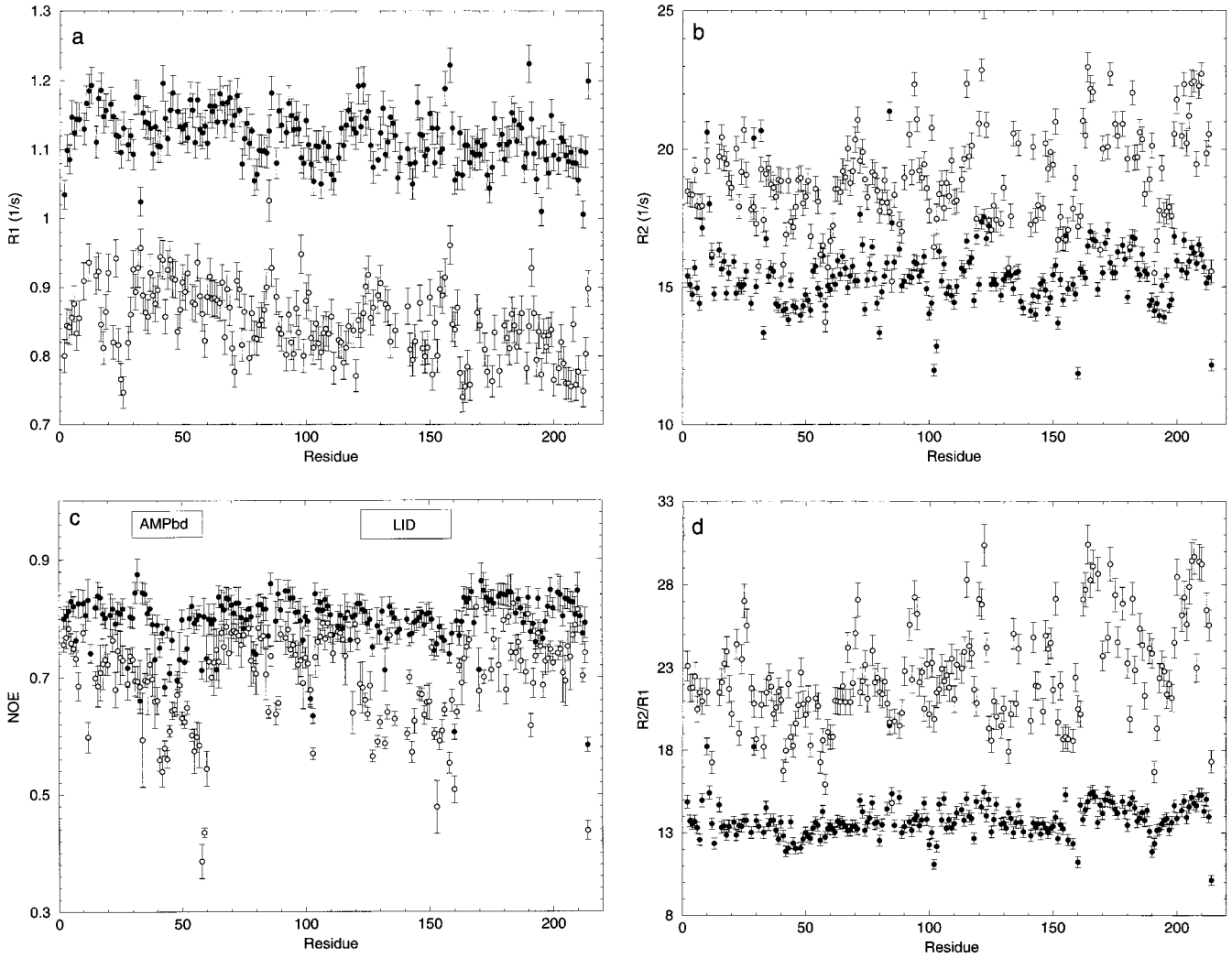

FIGURE 3: Relaxation parameters for AKeco (open circles) and AKeco*AP$_5$A (filled circles): (a) R_1, s^{-1}, (b) R_2, s^{-1}, (c) NOE, and (d) R_2/R_1.

solution with τ_m(app) = 15.05 ns. For this AKeco form we calculated $D_{parallel}/D_{perp}$ = 1.49 based on the inertia tensor and obtained $D_{parallel}/D_{perp}$ = 1.25 with NMR. Although τ_m(app) values on the order of 15 ns were determined in the past for 24 kDa proteins (*63*), in view of τ_m(app) of AKeco being substantially higher than τ_m(app) of AKeco*AP$_5$A, and $D_{parallel}/D_{perp}$ considerably smaller than predicted for a diffusive Debye particle, it was felt to be necessary to ascertain absence of detrimental protein association in the AKeco sample. Also, we examined analysis-related factors that might corrupt the diffusion tensor estimates.

Concentration-dependent relaxation measurements are, in principle, appropriate for testing protein self-association. However, we estimated the increase in τ_m(app) from 11.42 to 15.05 ns to be too small to obtain conclusive results using a quantitative approach (*64*). We therefore ascertained predominance of monomers for AKeco as follows. First, the spectroscopic manifestations of protein association are not borne out by the present data. As shown by Fushman et al. (*64*), an increase in dimer population implies a substantial increase in R_2/R_1, leaving the NOE magnitude and pattern virtually unchanged. In our case, we encountered a moderate increase in R_2/R_1 and a significantly different NOE pattern for AKeco as compared to AKeco*AP$_5$A (Figures 3, panels c and d). Second, size-exclusion chromatography experiments, described in the Experimental Procedures, were strongly supportive of a monomeric AKeco NMR sample. Third, fluorescence depolarization experiments on tryptophan residues of AKeco, carried out previously in the micromolar protein concentration range, gave τ_m(app) on the order of 15 ns (Haas, E. personal communication). A similar estimate for τ_m(app) at a concentration range 3 orders of magnitude lower than used in the NMR experiments suggests predominance of monomers in both AKeco samples. Finally, effects associated with R_{ex} contributions and ns motions, which may potentially impair the accuracy of the diffusion tensor estimates and thereby affect deduced microdynamic parameters, can be shown to be small for both AKeco forms. Thus, τ_m(app) will be overestimated if R_2 data with substantial R_{ex} contributions are not excluded from the calculation. However, in this case, the anisotropy of the diffusion tensor will be also overestimated (*65*), contrary to the $D_{parallel}/D_{perp}$ obtained in this study. To evaluate the effect of ns motions on the diffusion tensor estimate (*66*) of AKeco*AP$_5$A we used eqs 1 and 2 with $\langle\tau_s\rangle$ = 1.05 ns, $\langle S^2\rangle$ = 0.877, and $\langle S_f^2\rangle$ = 0.914, which are average values associated with model 5 spins. We found that ns motions contribute 7.8% to the R_1 values of 11% of the data and contribute marginally to R_2, with an insignificant effect on the diffusion tensor estimate. The contribution of ns motions to individual spins was found to

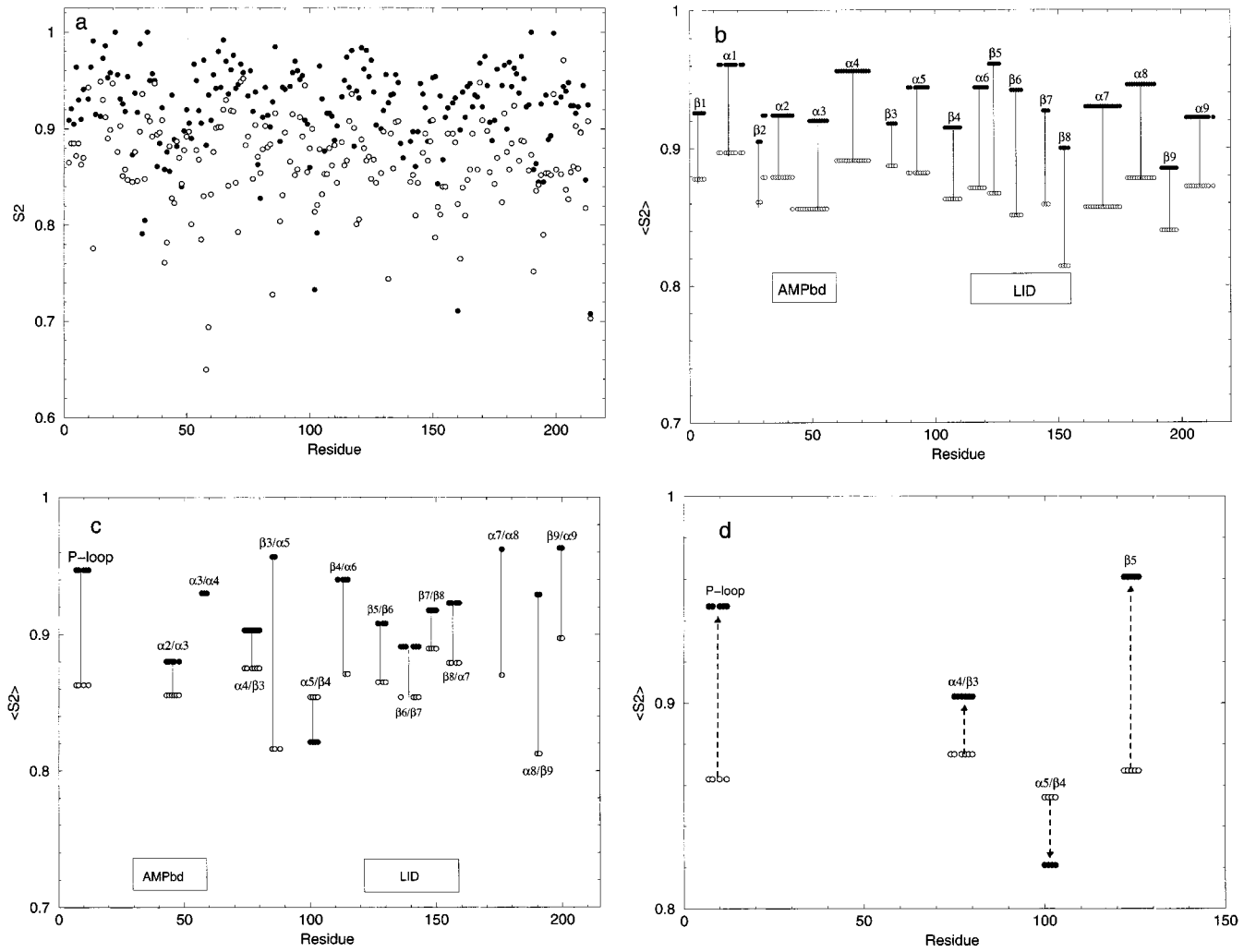

FIGURE 4: (a) Squared generalized order parameters, S^2, plotted as a function of residue number for AKeco (open circles) and AKeco*AP$_5$A (filled circles). (b) Weighted average S^2 values, $\langle S^2 \rangle$, for the various secondary structure elements of AKeco (open circles), and AKeco*AP$_5$A (filled circles). (c) $\langle S^2 \rangle$ for the various loops of AKeco (open circles), and AKeco*AP$_5$A (filled circles). (d) $\langle S^2 \rangle$ of loops P, α_4/β_3 and α_5/β_4, and strand β_5 for AKeco (open circles) and AKeco*AP$_5$A (filled circles). The average uncertainties are ± 0.016 for AKeco and ± 0.012 for AKeco*AP$_5$A. The data used are given in the Supporting Information.

be larger with AKeco, attaining 17% of R_1 in extreme cases. However, their overall effect on the diffusion tensor estimate was found to be small, as very similar results were obtained with and without spins associated with ns motions. We concluded that the detected differences in the overall diffusion tensors stem from intrinsic dynamic properties of the two AKeco forms.

Microdynamic Parameters. With AKeco*AP$_5$A, the relaxation parameters of 66, 59, 39, 5, and 30 residues were fit to models 1, 2, 3, 4, and 5, respectively, using $\alpha = 0.1$ critical value for χ^2 distribution, and $\alpha = 0.2$ critical value for *F*-statistic testing. With AKeco 2, 109, 7, 48, and 21 spins were fit to models 1, 2, 3, 4, and 5, respectively. The same statistical criteria as outlined above for AKeco*AP$_5$A were applied to 80% of the AKeco spins. For 7% of the spins, we used $\alpha = 0.05$ critical value for χ^2 distribution, and for 13% of the spins, the criteria for *F*-statistic testing were relaxed.

The globally optimized (*52*) microdynamic parameters of AKeco and AKeco*AP$_5$A obtained with these model classifications are compared below. The profiles of the squared generalized order parameters, S^2, of both AKeco forms are shown in Figure 4a. Mean S^2 values were calculated for individual α−helices, β-strands, and loops of AKeco and AKeco*AP$_5$A and plotted as a function of residue number in Figure 4, panels b and c. Loops have lower $\langle S^2 \rangle$ values than secondary structure elements in both AKeco forms. To elucidate the effect of ligand-binding on backbone dynamics we focused on *differences* in the $\langle S^2 \rangle$ values of corresponding secondary structure elements. The $\langle S^2 \rangle$ pattern of domain CORE is similar for both AKeco forms, whereas for domains AMPbd and LID it exhibits noteworthy differences. Loops α_2/α_3, α_4/β_3, β_5/β_4, β_5/β_6, β_6/β_7, β_7/β_8, and β_8/α_7 exhibit similar and relatively small changes in $\langle S^2 \rangle$. The differences in the $\langle S^2 \rangle$ values of loops P, β_3/α_5, α_7/α_8, α_8/β_9, and β_9/α_9 are significantly larger. It can be seen that the $\langle S^2 \rangle$ values of loops within CORE change to a significantly larger extent than the $\langle S^2 \rangle$ values of loops within LID. The $\langle S^2 \rangle$ values of secondary structure elements within CORE change to a smaller extent than the $\langle S^2 \rangle$ values of its loops, while the opposite is observed for domain LID. The smallest difference between the $\langle S^2 \rangle$ values of loops and secondary structure elements is featured by domain LID of AKeco.

The τ_e profile of the ligand-free form is shown in Figure 5a. The corresponding plot for the ligand-bound form features uniformly distributed τ_e values below 50 ps (Supporting

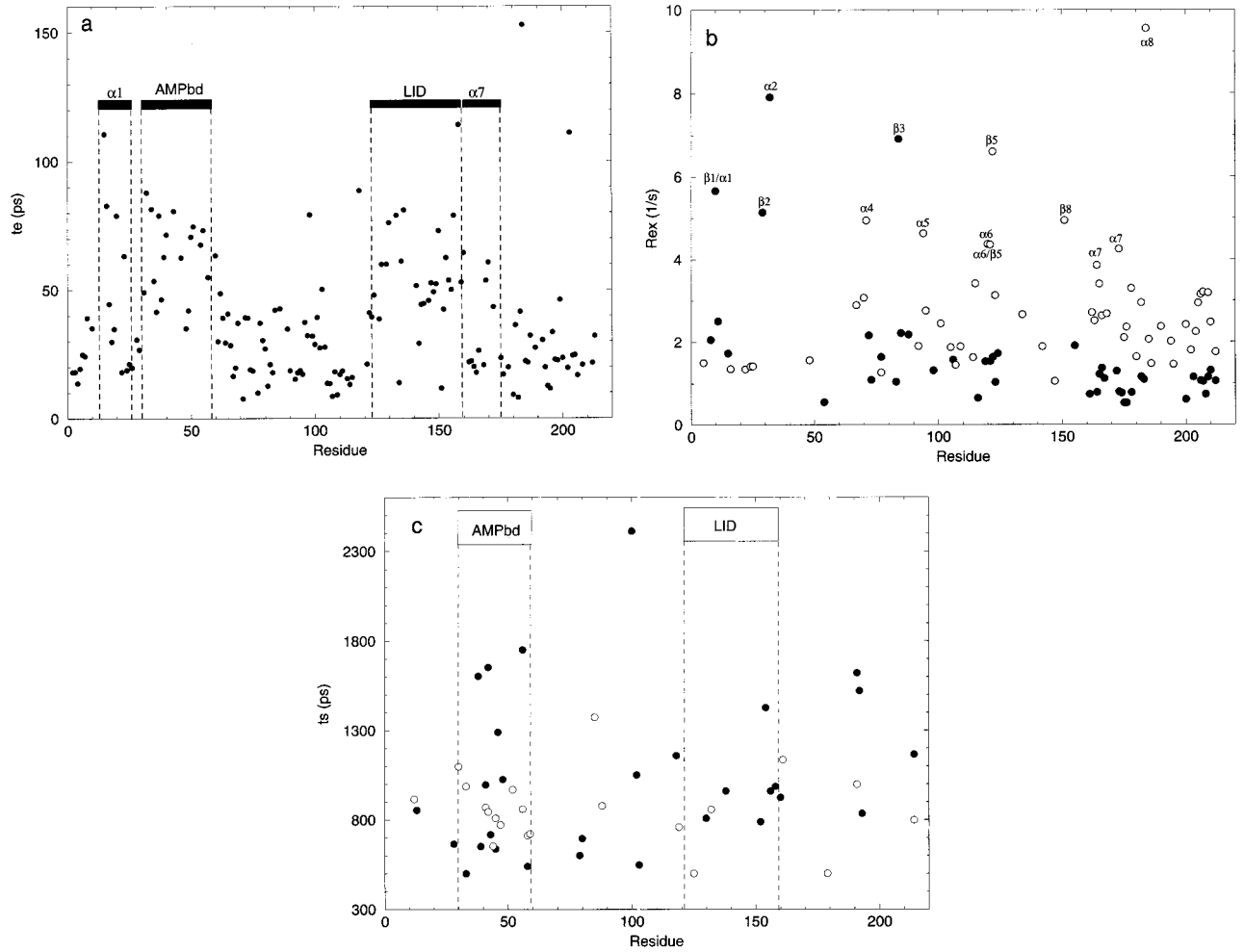

FIGURE 5: Microdynamic parameters for AKeco (open circles) and AKeco*AP_5A (filled circles). (a) Effective correlation time for fast internal motion τ_e, ps, for AKeco. (b) Exchange contributions R_{ex}, s^{-1} for AKeco (open circles) and AKeco* AP_5A (filled circles). (c) Effective correlation time for slow internal motion τ_s, ps for AKeco (open circles) and AKeco* AP_5A (filled circles). The data used are given in the Supporting Information.

Information). Values of τ_e exceeding 50 ps are associated primarily with AMPbd, LID, and helices α_1 and α_7. The latter are located at the N-terminus of domain AMPbd, and the C-terminus of domain LID, respectively. On average τ_e is reduced upon ligand binding.

Figure 5c shows the effective correlation time for slow internal motions, τ_s, associated with model 5. It can be seen that domain AMPbd features the highest density of model 5 residues, with $\langle\tau_s\rangle = 850$ ps ($\langle S_s^2\rangle = 0.95$ and $\langle S_f^2\rangle = 0.91$) for AKeco, and $\langle\tau_s\rangle = 1100$ ps ($\langle S_s^2\rangle = 0.97$ and $\langle S_f^2\rangle = 0.93$) for AKeco*$AP_5A$.

The R_{ex} terms are shown in Figure 5b. To evaluate exchange contributions independently of the Modelfree calculation, we measured ^{15}N-CSA$-^{15}$N-^{1}H dipolar cross-correlation rates η_{xy} (*44*). As pointed out in the context of the model-independent approach (*67*), in the absence of exchange contributions $\eta_{xy}-R_2$ correlations cluster about a straight line. Digressions to the right of the cluster on the η_{xy}/R_2 map are expected for residues with significant R_{ex} terms (*67*, *65*). The AKeco*AP_5A correlations G10, I29, G32, and D84 featured $R_{ex} > 4.5$ s^{-1}. Peak G32 was not detected in the η_{xy} experiment, and the remaining three correlations digressed substantially from the cluster, as shown in Figure 6b. Ten of thirteen AKeco*AP_5A correlations associated with $R_{ex} > 1.5$ s^{-1}, but none of the spins devoid of R_{ex} terms, were shifted considerably to the right. This confirms the modelfree-based identification of R_{ex} contributions for AKeco*AP_5A. Residues R71, D94, G122, E151, and K184 of AKeco were associated with R_{ex} contributions of 4.5−9.5 s^{-1}. Peak K184 was not detected in the η_{xy} experiment, correlations R71 and E151 did not digress, and correlation G122 (D94) digressed substantially (moderately) to the right of the cluster on the η_{xy}/R_2 map (Figure 6a). The other correlations marked in Figure 6a represent 8 of 22 correlations with $R_{ex} > 2.5$ s^{-1}. The results obtained with AKeco support the modelfree-based identification of R_{ex} terms in a much less definitive way than those obtained with AKeco*AP_5A. It is in order to note that helices α_7 and α_9 of both AKeco forms feature many contiguous residues with substantial R_{ex} contributions, possibly reflecting collective motion on the microsecond to millisecond time scale. This process appears to be suppressed upon inhibitor binding (Figure 5b).

DISCUSSION

Most aspects of spin relaxation associated with AKeco*AP_5A complied with expectations from globular proteins, in accordance with the previously reported rigidity of this molecular complex (*16*). On the other hand, AKeco featured several irregularities. For example, the ligand-free

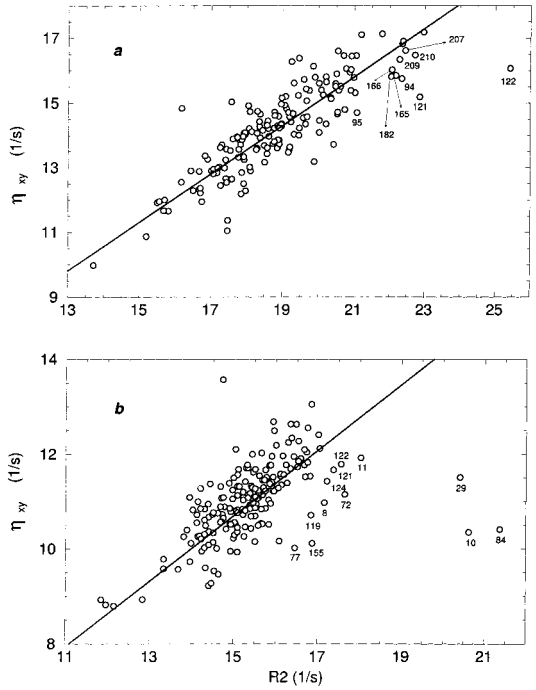

FIGURE 6: Correlation maps of the ^{15}N CSA-^{15}N-^{1}H dipolar cross-correlation rate, η_{xy}, and the transverse ^{15}N relaxation rate, R_2, for (a) AKeco and (b) AKeco*AP$_5$A. The AKeco residues marked in Figure 6a include G122 and D94 with $R_{ex} > 4.5$ s^{-1}, and residues with $R_{ex} > 2.5$ s^{-1}. The AKeco*AP$_5$A residues marked in Figure 6b include G10, I29, and D84 with $R_{ex} > 4.5$ s^{-1}, and residues with $R_{ex} > 1.5$ s^{-1}. The straight lines represent linear fits.

form did not bear out the expectation that the anisotropy of the diffusion tensor can be deduced with reasonable accuracy from the anisotropy of the inertia tensor of the crystal structure (*62*). This can be rationalized recalling that AKeco is a multiple-domain construct made of an intertwined chain, where individual domains execute in solution large-scale restricted motions relative to one another (*16*, *17*). This situation differs from cases where the individual domains are attached by flexible linkers, but tumble in solution as diffusive Debye particles (*5*, *33*). The AKeco molecule may not behave as a rigid-body Debye particle with independent fast internal motions. In particular, it may assume in solution an effective shape which is less anisotropic than the crystal structure. Restricted domain mobility actually materializes dynamic coupling between overall and internal motions, as opposed to decoupled dynamic modes postulated by the modelfree approach. This may influence the nature of the R_2/R_1 data set used for diffusion tensor calculations and the accuracy of the angles θ and ϕ. Deviations from a diffusive Debye model are also likely to underlie the lower performance of the model-independent method in identifying R_{ex} terms. Thus, internal motions may not be described properly by independent, small, equal amplitude restricted rotations about three mutually orthogonal axes (*44*). The irregularities featured by the ligand-free form of AKeco probably constitute digressions from the model-free and model-independent approaches. However, a Modelfree-type analysis generating physically tenable parameters is justified within the scope of a largely qualitative and comparative account. The individual domains of AKeco in the ligand-free and inhibitor-bound forms are discussed below.

Domain CORE. The τ_e values lie below 50 ps within domain CORE, and the respective profiles are quite uniform for both AKeco and AKeco*AP$_5$A. In general, the $\langle S^2 \rangle$ values of AKeco increase uniformly upon inhibitor binding. Several exceptions were identified. Thus, the $\langle S^2 \rangle$ values of loops α_4/β_3 and α_8/β_7 increase to a notably smaller extent, and loop α_5/β_4 is the only element of secondary structure for which $\langle S^2 \rangle$ decreases upon AP$_5$A binding (Figure 4c). Loops α_4/β_3 and α_5/β_4 are of particular interest. On the basis of *B*-factor analysis, Müller et al. (*10*) found that these loops exhibit higher (lower) flexibility than the catalytic site in the AKeco*AP$_5$A (AKeco) crystal structure. These observations underlie the hypothesis that upon substrate binding chain mobility increases in a region remote from the active center. As this region "solidifies" again upon substrate release, it serves as a "counterweight", balancing the substrate-binding energy. The $\langle S^2 \rangle$ values of loops α_4/β_3, α_5/β_4, P, and strand β_5, with the two latter elements pertaining to the binding site, are shown in Figure 4d. Subtracting the AKeco data from the corresponding AKeco*AP$_5$A data one obtains 0.085, 0.095, 0.03, and -0.04 for loops α_4/β_3, α_5/β_4, P, and strand β_5, respectively. This is in qualitative agreement with the *B*-factor-based hypothesis of Müller et al. (*10*). The *B*-factors of the two ligand forms are compared in Figure 2 of ref *10*, indicating that, except for loops P, α_4/β_3, and α_5/β_4, differences are generally small for domain CORE.

Domain LID. Domain LID features large differences between the $\langle S^2 \rangle$ values of the β-strands and small differences between the $\langle S^2 \rangle$ values of the intervening loops, while the opposite trend is observed within CORE. This highlights the intricate manner in which the polypeptide chain responds to ligand binding. Differences between the crystallographic *B*-factors of domain LID in the two AKeco forms (Figure 2 of ref *10*) also display a complex alternating pattern. The τ_e values of LID are comparable to those of AMPbd. With AKeco, they are higher than the τ_e values of CORE (Figure 5a) and become reduced to the level of the CORE values upon ligand binding. Thus, NMR provides evidence for binding-induced reduction in the entropic contribution of subnanosecond fluctuations to the stability of LID and AMPbd in the ligand-free form. Loop β_8/α_7, located at the C-terminus of domain LID, features dynamic properties similar to those of domain LID. Helix α_7 is associated with τ_e values comparable in magnitude to those within LID (Figure 5a). An abrupt decrease in S^2, observed with ^{15}N relaxation methods, is often associated with a hinge position (*68*). The S^2 profile shown in Figure 4a features a local minimum near residue D159, implied by the crystallographic studies to represent hinge H6 (*10*). The chain segment at the C-terminus of domain LID, including hinge H6, is likely to be involved in the catalysis-related movements of this domain.

Domain AMPbd. This domain is singled out by contiguous residues associated with model 5, featuring subnanosecond fluctuations characterized by S_f^2 and nanosecond motions characterized by S_s^2 and τ_s. All of these parameters increase on average (Figure 5c), whereas τ_e decreases (Figure 5a) upon inhibitor binding. Thus, inhibitor binding affects AMPbd dynamics in an intricate manner. It also induces unique structural changes, by causing unwinding of the N-terminus of helix α_3 (*9*, *10*). Helix α_1, which includes part of loop P, has τ_e values comparable with those of AMPbd (Figure 5a). This is quite intriguing, providing evidence for dynamic correlation between the nucleotide-binding motif

denoted as P-loop and the catalysis-related movements of domain AMPbd. The S^2 profile shown in Figure 4a features a local minimum near residue V59, implied by the crystallographic studies to be hinge H4 (*10*).

Catalytic Site. Residues G10, I29, G32, and D84, which feature the largest exchange contributions in AKeco*AP_5A, are spatially close to the intermolecular hydrogen bond network between AP_5A and the enzyme in the crystal structure (*9*). The observed R_{ex} terms can be interpreted assuming that the binding-site-related hydrogen-bond network prevails in solution in dynamic equilibrium, modulating the magnetic environments of several spatially proximal ^{15}N nuclei. Similar observations were made by Nicholson et al. (*69*) for inhibitor-bound HIV-1 protease. Residue G10 binds directly to the inhibitor (*9*). It is the only member of the binding-site-related hydrogen-bond network with a large R_{ex} term, possibly related to the rate of hydrogen-bond reorganization. Since this dynamic process is necessarily discontinued upon product release, residue G10 of the nucleotide-binding P-loop motif might play a role in kinase catalysis. Note that exchange broadening due to AKeco*AP_5A dissociation was shown to be negligible (*23*).

Among 21 ^{15}N-^1H backbone correlations that change marginally upon inhibitor binding (Figure 2), 10 pertain to the LID domain. Empirically, this points out structural preservation throughout the large catalysis-related displacement of this domain. On the other hand, as outlined above, the dynamic properties of domain LID change significantly upon inhibitor binding. It has been postulated (*12*, *70*) that domain LID functions by regulating entropically both termination of catalysis and product release. The relation between these functions and the microscopic parameters elucidated in this study is yet to be determined.

In summary, domains AMPbd and LID of AKeco experience pervasive subnanosecond fluctuations suppressed upon AP_5A-binding, and domain AMPbd is engaged in nanosecond motions in both AKeco form. The chain segments N-terminal to AMPbd and C-terminal to LID appear to be involved in the catalysis-related domain movements. The $\langle S^2 \rangle$ profiles of secondary structure elements and loops respond to ligand binding in an intricate way. The hypothesis of "energetic counterbalancing of substrate binding" is supported by our NMR data.

Prospects of this research include the usage of perdeuterated samples, concerted analysis of data acquired at several magnetic fields, and the development of enhanced dynamic models.

ACKNOWLEDGMENT

The authors wish to thank Prof. Elisha Haas for supporting this project. We gratefully acknowledge Prof. A. Wittinghofer (Max-Planck-Institute for Molecular Physiology, Dortmund, Germany) for the recombinant plasmid pEAK91 gift. We thank Dr. Frank Delaglio for the use of his software packages nmrPipe and modelXY. We also thank Mrs. Tatyana Shapiro for help with manuscript preparation.

SUPPORTING INFORMATION AVAILABLE

HN and ^{15}N assignments, R_1 and R_2 ^{15}N relaxation rates and steady-state ^{15}N-$\{^1H\}$ NOEs (Table S1), and microdynamic ^{15}N relaxation parameters (Table S2) for AKeco at 303K. R_1 and R_2 ^{15}N relaxation rates and steady-state ^{15}N-$\{^1H\}$ NOEs (Table S3), and microdynamic ^{15}N relaxation parameters (Table S4) for AKeco*AP_5A at 303K. This material is available free of charge via the Internet at http://pubs.acs.org.

REFERENCES

1. Bennett, W. S., and Huber, R. (1984) *Crit. Rev. Biochem. 15*, 291−384.
2. Sicheri, F., and Kuriyan, J. (1997) *Curr. Opin. Struct. Biol. 7*, 777−785.
3. Mayer, B. J., Hirai, H., and Sakai, R. (1995) *Curr. Biol. 5*, 296−305.
4. Cambell, I. D., and Downing, A. K. (1998) *Nat. Struct. Biol. 5* (Suppl.), 496−499.
5. Fushman, D., Xu, R., and Cowburn, D. (1999) *Biochemistry 38*, 10225−10230.
6. Gerstein, M., Lesk, A. M., and Chothia, C. (1994) *Biochemistry 33*, 6739−6749.
7. Noda, L. (1973) in *The Enzymes* (Boyer, P. D., Ed.) Vol. 8, pp 279−305.
8. Vornhein, C., Schlauderer, G. J., and Schulz, G. (1995) *Structure 3*, 483−490.
9. Müller, C. W., and Schulz, G. (1992) *J. Mol. Biol. 224*, 159−177.
10. Müller, C. W., Schlauderer, G. J., Reinstein, J., and Schulz, G. (1996) *Structure 4*, 147−156.
11. Anderson, C. M., Zucker, F. H., and Steiz, T. A. (1979) *Science 204*, 375−380.
12. Berry, M. B., Meador, B., Bilderback, T., Liang, P., and Glaser, M. (1994*) Proteins: Struct., Funct., Genet. 19*, 183−198.
13. Schulz, G., Müller, C. W., and Deiderichs, K. (1990) *J. Mol. Biol. 213*, 627−630.
14. Müller-Dickermann, H.-J., and Schulz, G. E. (1995) *J. Mol. Biol. 246*, 522−530.
15. Richard, J. P., and Frey, P. A. (1978) *J. Am. Chem. Soc. 100*, 7757−7758.
16. Sinev, M. A., Sineva, E. V., Ittah, V., and Haas, E. (1996) *Biochemistry 35*, 6425−6437.
17. Sinev, M. A., Sineva, E. V., Ittah, V., and Haas, E. (1996) *FEBS Lett. 397*, 273−276.
18. Vetter, I., Konrad, M., and Rosch, P. (1991) *Biochemistry 30*, 4137−4142 and references therein.
19. Byeon, I.-J., Yan, H., Edison, A. S., Mooberry, E. S., Abildgaard, F., Markley, J, L., and Tsai, M.-D. (1993) *Biochemistry 32*, 12508−12521.
20. Byeon, I.-J., Shi, Z., and Tsai, M.-D. (1995) *Biochemistry 34*, 3172−3182.
21. Burlacu-Miron, S., Perrier, V., Gilles, A.-M., Pistotnik, E., and Craescu, C. T. (1998) *J. Biol. Chem. 273*, 19102−19107.
22. Burlacu-Miron, S., Perrier, V., Gilles, A.-M., Mispelter, J., Barzu, O., and Craescu, C. T. (1999) *J. Biomol. NMR 13*, 93−94.
23. Burlacu-Miron, S., Gilles, A. M., Popescu, A., Barzu, O., and Craescu, C. T. (1999) *Eur. J. Biochem. 264*, 765−774.
24. Peng, J. W., and Wagner, G. (1994) in *Methods in Enzymology* (James, T. L., and Oppenheimer, N. J., Eds.) Vol. 239, pp 563−595, Academic Press, New York.
25. Abragam, A. (1961) *Principles of Nuclear Magnetism*, Oxford University Press, London.
26. Bloom, M., Reeves, L. W., and Wells, E. J. (1965) *J. Chem. Phys. 42*, 1615−1625.
27. Lipari, G., and Szabo, A. (1982) *J. Am. Chem. Soc. 104*, 4546−4559.
28. Lipari, G., and Szabo, A. (1982) *J. Am. Chem. Soc. 104*, 4559−4570.
29. Clore, G. M., Szabo, A., Bax, A., Kay, L. E., Driscoll, P. C., and Gronenborn, A. M. (1990) *J. Am. Chem. Soc. 112*, 4989−4991.
30. Clore, G. M., Driscoll, P. C., Wingfield, P. T., and Gronenborn, A. (1990) *Biochemistry 29*, 7387−7401.
31. Tjandra, N., Feller, S. E., Pastor, R. W., and Bax, A. (1995) *J. Am. Chem. Soc. 117*, 12562−12566.

32. Zheng, Z., Czaplicki, J., and Jardetzky, O. (1995) *Biochemistry 34*, 5212−5223.
33. Brüschweiler, R., Liao, X., and Wright, P. E. (1995) *Science 268*, 886−889.
34. Lee, L. K., Rance, M., Chazin, W. J., and Palmer, A. G., III (1997) *J. Biomol. NMR 9*, 287−298.
35. Reinstein, J., Brunne, M., and Wittinghofer, A. (1988) *Biochemistry 27*, 4712−4720.
36. Girons, I. S., Gilles, A.-M., Margarita, D., Michelson, S., Monnot, M., Fermandjian, S., Danchin, A., and Barzu, O. (1987) *J. Biol. Chem. 262*, 622−629.
37. Delaglio, F., Grzesiek, S., Vuister, G. W., Zhu, G., Pfeifer, J., and Bax, A. (1995) *J. Biomol. NMR 6*, 277−293.
38. Vold, R. L., Waugh, J. S., Klein, M. P., and Phelps, D. E. (1968) *J. Chem. Phys. 48*, 3831−3832.
39. Meiboom, S., and Gill, D. (1958) *Rev. Sci. Instrum. 29*, 688−691.
40. Noggle, J. H., and Shirmer, R. E. (1971) *The Nuclear Overhauser Effect: Chemical Aplications*, Academic Press, New York.
41. Kay, L. E., Nicholson, L. K., Delaglio, F., Bax, A., and Torchia, D. A. (1992) *J. Magn. Reson. 97*, 359−375.
42. Palmer, A. G., III, Skelton, N. J., Chazin, W. J., Wright, P. E., and Rance, M. (1992) *Mol. Phys. 75*, 699−711.
43. Grzesiek, S., and Bax, A. (1993) *J. Am. Chem. Soc. 115*, 12593−12594.
44. Tjandra, N., Szabo, A., and Bax, A. (1996) *J. Am. Chem. Soc. 118*, 6986−6991.
45. Live, D. H., Davis, D. G., Agosta, W. C., and Cowburn, D. (1984) *J. Am. Chem. Soc. 106*, 1939−1941.
46. Palmer, A. G., III, Rance, M., and Wright, P. E. (1991) *J. Am. Chem. Soc. 113*, 4371−4380.
47. Brünger, A. T. (1992) X-PLOR, Version 3.1. *A System for X-ray Crystallography and NMR*, Yale University Press, New Haven, CT.
48. Hyiama, Y., Niu, C. H., Silverton, J. V., Bavaso, A., and Torchia, D. A. (1988) *J. Am. Chem. Soc. 110*, 2378−2383.
49. Fushman, D., Tjandra, N., and Cowburn, D. (1998) *J. Am. Chem. Soc. 120*, 10947−10952.
50. Fushman, D., and Cowburn, D (1999) *J. Biomol. NMR 13*, 139−147.
51. Kroenke, C. D., Rance, M., and Palmer, A. G., III (1999) *J. Am. Chem. Soc. 121*, 10119−10125.
52. Mandel, A. M., Akke, M., and Palmer, A. G., III (1995) *J. Mol. Biol. 246*, 144−163.
53. Bodenhausen, G., and Ruben, D. J. (1980) *Chem. Phys. Lett. 69*, 185−189.
54. Marion, D., Driscoll, P. C., Kay, L. E., Wingfield, P. T., Bax, A., Gronenborn, A. M., and Clore, G. M. (1989) *Biochemistry 28*, 6150−6156.
55. Marion, D., Kay, L. E., Sparks, S. W., Torchia, D. A., and Bax, A. (1989) *J. Am. Chem. Soc. 111*, 1515−1517.
56. Zuiderweg, E. R. P., and Fesik, S. W. (1989) *Biochemistry 28*, 2387−2391.
57. Vuister, G. W., and Bax, A. (1993) *J. Am. Chem. Soc. 115*, 7772−7777.
58. Meirovitch, E., Sinev, M. A., and Sineva, E. V. (1999) *J. Biomol. NMR 13*, 195−196.
59. Zhang, P., Dayie, K., and Wagner, G. (1997) *J. Mol. Biol. 272*, 443−455.
60. Yao, S., Hinds, M. G., and Norton, R. S. (1998) *J. Magn. Reson. 131*, 347−350.
61. Shapiro, Yu. E., Gorbatyuk, V. Ya., Levashov, A. V., and Klyachko, N. L. (1994) *Biol. Membr. 7*, 277−290.
62. Copie, V., Tomita, Y., Akiyama, S. K., Aota, A., Yamada, K. M., Venable, R. M., Pastor, R. W., Krueger, S., and Torchia, D. A. (1998) *J. Mol. Biol. 277*, 663−682.
63. Wagner, G. (1997) *Nat. Struct. Biol. 5* (Suppl.), 841−844.
64. Fushman, D., Cahill, S., and Cowburn, D. (1997) *J. Mol. Biol. 266*, 173−194.
65. De Alba, E., Baber, J. L., and Tjandra, N. (1999) *J. Am. Chem. Soc. 121*, 4281−4283.
66. Korzhnev, D. M., Orekhov, V. Y., and Arseniev, A. S. (1997) *J. Magn. Reson. 127*, 184−191.
67. Fushman, D., and Cowburn, D. (1998) *J. Am. Chem. Soc. 120*, 7109−7110.
68. Carr, P. A., Erickson, H. P., and Palmer, A. G., III (1997) *Structure 5*, 949−959.
69. Nicholson, L. K., Yamazaki, T., Torcia, D. A., Grzesiek, S., Bax, A., Stahl, S. J., Kaufman, J. D., Wingfield, P. T., Lam, P. Y. S., Jadhav, P. K., Hodge, C. N., Domaille, P. J., and Chang, C.-H. (1995) *Struct. Biol. 2*, 274−279.
70. Berry, M. B., and Phillips, G. N. (1988) *Proteins: Struct., Funct., Genet. 32*, 276−288.
71. Kraulis, P. J. (1991) Molscript: A Program to Produce both Detailed and Schematic Plots of Protein Structures. *J. Appl. Crystallogr. 24*, 946−995.

BI992076H